Article:
Radtke, G, Hennes, M, Bugnet, M et al. (2019) Atomic-Scale Study of Metal–Oxide Interfaces and Magnetoelastic Coupling in Self-Assembled Epitaxial Vertically Aligned Magnetic Nanocomposites. Advanced Materials Interfaces, 6 (17). 1900549. ISSN: 2196-7350

https://doi.org/10.1002/admi.201900549

Atomic-Scale Study of Metal-Oxide Interfaces and Magneto-Elastic Coupling in Self-Assembled Epitaxial Vertically Aligned Magnetic Nanocomposites

Guillaume Radtke, Marcel Hennes, Matthieu Bugnet, Quentin M. Ramasse, Xiaorong Weng, Dominique Demaille, Benoit Gobaut, Philippe Ohresser, Edwige Otero, Fadi Choueikani, Amélie Juhin, Philippe Sainctavit, Yunlin Zheng, and Franck Vidal**

Dr. G. Radtke, Dr. A. Juhin, Dr. Ph. Sainctavit
CNRS, Sorbonne Université, IRD, MNHN, Institut de Minéralogie, Physique des Matériaux et de Cosmochimie, IMPMC UMR7590, F-75005 Paris, France
*E-mail: guillaume.radtke@sorbonne-universite.fr

Dr. M. Hennes, X. Weng, Dr. D. Demaille, Dr. Y. Zheng, Dr. F. Vidal
Sorbonne Université, CNRS, Institut des NanoSciences de Paris, INSP, F-75005 Paris, France,
*E-mail: franck.vidal@insp.jussieu.fr

Dr. M. Bugnet
Université de Lyon, INSA Lyon, UCBL Lyon 1, MATEIS, UMR 5510 CNRS, 69100 Villeurbanne Cedex, France

Dr. Q. Ramasse
SuperSTEM Laboratory, STFC Daresbury Campus, Daresbury WA4 4AD, United Kingdom,

Pr. Q. Ramasse
School of Physics and School of Chemical and Process Engineering, University of Leeds, Leeds LS2 9JT, United Kingdom

Dr. B. Gobaut, Dr. P. Ohresser, Dr. E. Otero, Dr. F. Choueikani, Dr. Ph. Sainctavit
Synchrotron Soleil, L'Orme des Merisiers Saint-Aubin BP 48, 91192 Gif-sur-Yvette Cedex, France

Keywords: interfaces, magnetic nanocomposites, electron microscopy, electron energy loss spectroscopy, x-ray magnetic dichroism

Vertically aligned nanocomposites (VANs) of metal/oxide type have recently emerged as a novel class of heterostructures with great scientific and technological potential in the fields of nanomagnetism, multiferroism and catalysis. One of the salient features of these hybrid materials is their huge vertical metal/oxide interface, which plays a key role in determining the final magnetic and/or transport properties of the composite structure. However, in contrast to their well-studied planar counterparts, detailed information on the structural features of

vertical interfaces encountered in VANs is scarce. In this work, high resolution scanning transmission electron microscopy (STEM) and electron energy-loss spectroscopy (EELS) are used to provide an element selective, atomic-scale analysis of the interface in a composite consisting of ultrathin, self-assembled Ni nanowires, vertically epitaxied in a $SrTiO_3/SrTiO_3(001)$ matrix. Spectroscopic EELS measurements evidence rather sharp interfaces (6-7 Å) with the creation of metallic Ni-Ti bonds and the absence of nickel oxide formation is confirmed by x-ray absorption spectroscopy measurements. The presence of these well-defined phase boundaries, combined with a large lattice mismatch between the oxide and metallic species, gives rise to pronounced magneto-elastic effects. Self-assembled columnar $Ni:SrTiO_3$ composites thus appear as ideal model systems to explore vertical strain engineering in metal/oxide nanostructures.

1. Introduction

Vertically aligned nanocomposites (VANs) form a class of hybrid thin films,[1,2] that has attracted significant interest since the discovery of self-assembled vertical nanopillar microstructures in the $La_{0.67}Ca_{0.33}MnO_3:MgO$ system.[3] Possible applications for these heterostructured materials have been proposed in the fields of nanomagnetism,[4] spintronics,[5,6] multiferroics,[7-14] catalysis and ionic conductors.[15] The versatility of VANs results from their peculiar nanoarchitecture: they are composed of an array of nanopillars vertically embedded and epitaxially coupled to a surrounding single crystal matrix, which is depicted schematically in **Figure 1** for the case of the particular combination of materials studied in this work. While initial work on the growth of VANs reported the successful synthesis of vertical metallic nanostructures in an oxide host ($Fe:LaSrFeO_4$, [16]) most of the attention turned to oxide/oxide VANs in the following years, driven by the wide range of functionalities available in oxide materials and the good structural compatibility between

spinel and perovskite structures. In particular, ferroelectric/ferrimagnetic VANs were intensively studied with the aim of coupling the ferroic properties in an artificial multiferroic material.[7-14]

Recent years however have seen the emergence of a variety of studies on metal/oxide VANs coupling transition or noble metals with oxide host matrices. The successful growth of nanocomposites consisting of elemental Fe, Ni, Co, Au, Pt, Ir nanorods, as well as of Co_xNi_{1-x} alloys, epitaxied in $SrTiO_3$ (STO), $BaTiO_3$, $BaZrO_3$, or CeO_2 thin films was demonstrated.[17-26] Like their oxide/oxide counterparts, metal/oxide VANs are of interest in many areas: Au:$BaTiO_3$ VAN systems are appealing in the field of optical metamaterials,[23] Pt:STO and Ir:STO VANs were demonstrated to exhibit enhanced activity in photoelectrochemical water splitting,[22] VANs incorporating Fe, Ni or Co transition metals display interesting properties such as large perpendicular magnetic anisotropy potentially appealing for the development of materials for data storage.[19,20,24]

The large interface/volume ratio is a salient feature of the VAN nanoarchitecture and the vertical interface between the pillars and the surrounding matrix plays a prominent role in determining the final functionality of the nanocomposite. For example, the vertical interface can provide additional conduction channels in ionic conductors; the photocarrier transport can be more efficient due to the Schottky junctions around metallic pillars embedded in a semiconducting matrix; efficient magneto-elastic coupling through epitaxial strain is intimately related to the structure of the vertical interface.[27,28]

The metal/oxide interface results from the immiscibility of the two phases, but grows in out-of-equilibrium conditions. Its structure/composition may thus reflect the fact that the system is stuck in a metastable state. In addition, the creation of interfacial compounds might also be envisioned. As a consequence, the interfacial region may not be as sharp as in oxide/oxide systems. Despite the crucial role played by the vertical interface, studies addressing its

structure/composition at the atomic scale are scarce, possibly due to the difficulty to access the interface compared to more conventional planar heterostructures.[27-30]

In this work, we therefore present an atomic-scale analysis of metal/oxide interfaces using Ni:$SrTiO_3$ VANs (Ni:STO) as a model system. Ni:STO VANs have been extensively studied recently, from both a theoretical and an experimental point of view. The initial growth stages of this composite were simulated using a kinetic Monte-Carlo approach based on density functional theory.[25] The interfaces observed in this study were sharp, but these results must be considered with care, as the underlying coarse-grained model might not be able to grasp the atomic details of the interface structure. In a more recent study, a detailed analysis of the structure of the nanocomposite was given, unveiling a tilting relaxation mechanism as well as a possible amorphization of the embedded metallic structure upon diameter reduction.[26] No experimental data on the chemical composition of the interface is available yet. In the present paper, we combine scanning transmission electron microscopy (STEM), atomic resolution electron energy-loss spectroscopy (EELS) with x-ray magnetic circular dichroism (XMCD) and conventional magnetometry measurements to show that the interfaces do not present any sign of oxidation and show only very weak interdiffusion, two essential prerequisites to eventually obtain pronounced magneto-elastic coupling effects.

2. Results and discussion

A global view of the sample, observed along the [001] zone axis of the STO matrix, is displayed in **Figure 2**(a). The High Angle Annular Dark Field (HAADF) contrast reveals a set of bright, well separated Ni nanowires of diameter close to 2 nm in the midst of the STO matrix, distant from each other by about 10 to 20 nm. A number of smaller diameter, shorter wires do not reach the surface of the cross-sectional sample, such that the STO and Ni lattices appear superimposed. The faceted nanowire visible at the center of the image is presented at

higher magnification in Figure 2(b), and was used as a prototypical object for the atomic-scale spectroscopic investigations presented in the remainder of this work. The metal/oxide interface is structurally abrupt with no visually detectable phase reaction between the two materials. Epitaxial strain indicative of a partially coherent interface between the nanowire and the matrix is visible through the deformation of the Ni lattice planes. Atomic-resolution elemental maps acquired on this nanowire are presented in Figure 2(d), (e) and (f) for Ti, O and Ni, respectively. A composite map summarizing these results is shown in (c). Chemical profiles extracted from these maps and obtained by integrating the signal in a vertical box shown in inset are presented in **Figure 3**. These profiles reveal a chemical width of the interface of about 0.6 nm when integrated over the thickness of the sample. The chemical interface is therefore larger that the apparently more abrupt structural interface contrast observed on the HAADF images. A sizeable intermixing is therefore clearly detected at the interface even if one accounts for the inelastic delocalization of the EELS signal caused by the long-ranged Coulomb interaction, estimated between 0.1 and 0.2 nm for edges of a few hundreds of eV,[31] and which leads inevitably to a broadening of the profiles. Very interestingly, a slight difference of 0.4 nm (i.e. 0.2 nm per interface) is observed between the global widths of the Ti and the O profiles. This is indicative of an increase of the Ti/O ratio at the interface with respect to the STO matrix and thus reveals a Ti-rich, or O-deficient, interface. Note that this effect is observed all along the interface and therefore, cannot be attributed to a geometrical tilt of the nanowire along a particular direction. As shown in Figure S1, this effect is indeed also visible on the $[110]_{STO}\|[110]_{Ni}$ facets oriented at 45°.

To go beyond this elemental analysis, spectrum images recorded with a higher energy resolution (~160 meV) have been acquired at the Ni-$L_{2,3}$, Ti-$L_{2,3}$ and O-K edges to monitor the spatial variation of their fine structures at the nanowire/matrix interface. The results are summarized in **Figure 4**, where the different regions of the spectrum images shown in (a)

have been used to extract the spectra displayed in (b), (c) and (d). Beginning at the bottom of Figure 4(c), (d), we first present reference edges (black solid lines) of bulk STO recorded in the matrix. The Ti-$L_{2,3}$ edges are characteristic of Ti^{4+} ($3d^0$) in octahedral environment,[32] where the $2p$ hole spin-orbit coupling splits the edge into a lower-lying L_3 and a higher-lying L_2 components. These two edges are further split into two t_{2g} and e_g components as a consequence of the octahedral crystal-field acting on the Ti-3*d* unoccupied states. This crystal-field splitting is echoed in peaks *a* and *b* at the onset of the O-*K* edge,[33–35] which reflects the O-*p* component of the t_{2g} and e_g hybridized states dominating the bottom of the conduction band of STO. Diffuse O-*p* orbitals further hybridize with the high-lying Sr-4*d* states leading to the formation of the double structure *c* at about 7-8 eV above the edge onset. The first series of spectra extracted from region A, on a TiO_2 atomic plane located at one matrix unit cell (~ 3.9 Å) from the interface, still displays all the characteristic features of the bulk electronic structure of STO without any detectable Ni. On the contrary, spectra from region B, located on the last atomic plane which can still be considered as belonging to the matrix from the HAADF contrast, are largely modified. The symmetry breaking induced by the presence of the interface as well as the pronounced covalent character of the bonding with neighboring metal atoms contrasting with the predominantly ionic bonding in STO, lead to a strong broadening of the Ti-$L_{2,3}$ edges fine structure where the t_{2g}/e_g splitting is barely resolved. The fine structure of the O-*K* edge still exhibits the signature of an hybridization with Ti-3*d* states through the presence of a sharp peak a and a broader structure b. Interestingly, the missing SrO plane on the left side of the interface leads to a considerable loss of spectral weight in the region of the double structure c, primarily associated with the Sr-4*d* empty states. Note that a weak Ni signal is already detected in this region, consistently with the elemental profiles shown in Figure 3. As already discussed, although this signal

might be partly related to the delocalization inherent to EELS, the presence of Ni in the last atomic planes of the matrix cannot be ruled out.

Note that while the modification of the Ti-$L_{2,3}$ edges fine structure is particularly abrupt along this $[100]_{STO}\|[100]_{Ni}$ interface, it occurs in a more gradual manner for the $[110]_{STO}\|[110]_{Ni}$ facets where the Ti environment in the last atomic plane of the matrix is qualitatively closer to the bulk. Figure S2 presents a comparison of the spectra obtained for these two types of facets in the vicinity of the interface with the nanowire, and shows that in the latter case, the crystal-field splitting of the Ti-3*d* states is still clearly visible whereas it almost disappeared in the former.

Region C corresponds to the first atomic plane, which can be considered structurally as a part of the nanowire from the HAADF contrast. Consequently, a large increase of the Ni signal is observed with respect to region B. A comparison with a reference spectrum from bulk Ni[36,37] shown in Figure S3(a) reveals that, despite the relatively low signal-to-noise ratio of these spatially resolved data, a substantial broadening of the L_3 edge is clearly observed. This effect might be attributed to fluctuations of Ni oxidation state and local environment within the thickness of the specimen both in terms of geometry due to the presence of the metal/oxide interface and to the local disorder associated with the diffusion of Ti and O in the first atomic planes of the nanowire. The Ti-$L_{2,3}$ edges in this area is also further broadened to reach a shape which closely resembles that of the Ti-$L_{2,3}$ edges in bulk Ti or NiTi alloy.[36] A comparison between this Ti-$L_{2,3}$ and a reference spectrum[37] recorded in bulk Ti is presented in Figure S3(b). The O-*K* edge also displays broader structures when compared to region B, however retains its global shape without displaying any particular new features.

In region D, the Ni- $L_{2,3}$ edges are essentially that of bulk Ni (see Figure S3(a)), while very weak Ti and O signals are still detectable. Finally, regions E and F are characteristic of pure bulk Ni. The Ni-L_3 to L_2 ratios extracted from these data are presented in Figure 4(e), the

procedure employed to obtain these values is detailed in Figure S4. Although the reduced signal-to-noise ratio inherent to these spatially resolved data limits the accuracy of the results, no substantial deviation from the bulk Ni value is observed in this series of spectra.

In summary, no reaction phase could be detected at the metal/oxide interface. While structurally abrupt, spectroscopic investigations at the atomic-scale indicate however the presence of a weak interdiffusion occurring over a few atomic planes only. This leads essentially to a metallization of the last TiO_x ($x< 2$) atomic plane of the matrix and to the formation of a few atomic planes of a non-stoichiometric mixed Ni-Ti oxide on the external part of the nanowire. Despite the presence of detectable O in these planes, the metal $L_{2,3}$ edges closely resemble those observed in bulk Ti or Ti intermetallics. This is consistent with the O-*K* edge fine structure at the interface, which does not display any characteristic features typically found in NiO.[38] Unlike in the case of a previous study carried out on a Ni thin film epitaxially grown on a STO(001) surface,[39] no evidence of the presence of a stoichiometric NiO layer could be found at the interface here. The results rather evidence the formation of metallic Ni-Ti bonds at the interface between the nanowire and the matrix. In previous work, a phenomenon was reported whereby some structural disorder could be detected within wires with diameters reduced below 2 nm.[26] In light of the present results, we suggest that the interdiffusion of Ti at the Ni:STO interface could contribute to this disordering process in ultrathin nanowires.

While the EELS results presented so far provide clear evidence for the preservation of the metallic character of the embedded Ni nanostructures, the analysis is limited to a very small number of nanowires, due to the intrinsic working principle of STEM-EELS as a highly local probe. To exclude any bias, Ni-STO VANs were thus further analyzed with x-ray absorption spectroscopy at the Ni-$L_{2,3}$ edges, providing insight into the nature of chemical bonding of Ni atoms on a global, sample-wide scale. **Figure 5**(a) shows the x-ray absorption data of a Ni-

STO VAN containing nanowires with mean diameter d=5 nm. The spectrum is very similar to those of earlier studies of bulk Ni,[42,43] with an absence of spectral features related to nickel oxide formation. Note for example the presence of a broad satellite peak located 6 eV above the L_3 maximum, which has been reported in other studies on metallic Ni.[42] The calculated Ni-L_3 to L_2 ratio (ratio of the integrated intensities) is 3.1 and matches, within error bars, the one determined previously by EELS measurements of the VAN with 2.4 nm diameter wires. It is also in good agreement with values reported in the literature.[43] This spectrum thus confirms the EELS data and, considering the surface sensitivity of the total electron yield (TEY) mode, also shows that an ultrathin AlO_x capping layer can be efficiently used to prevent oxidation at the apex of the wires.

The results show that NiO is efficiently reduced at the TiO_2-terminated interface with STO, leading to the formation of metallic Ni during the growth under vacuum. This can be attributed to the higher reactivity of the TiO_2-terminated surface of STO with respect to the more stable SrO-terminated surface.[44] This is a consequence of the fact that Sr levels are located deeper below the Fermi level than Ti and O levels that form the valence and conduction bands of STO.[45] This leads to a less reactive SrO surface with lower surface energy. In the case of Pt growth on $SrTiO_3$(001), the SrO-terminated surface has been shown to give rise to a weaker bonding with Pt than the TiO_2-terminated surface.[46] As NiO reduction at TiO_2-terminated interface with STO is a key step in the formation of the VAN, growth has to be performed under vacuum in order to favor this reaction. Under such conditions, we anticipate that using a mixed NiO-STO target or a Ni metallic target instead of NiO would lead to Ni:STO VAN formation as well. Other possible pairs of transition metal/oxide matrix, such as Co and CoNi alloys in $SrTiO_3$ and in $BaTiO_3$, may lead to VAN formation through the same mechanisms for which reduction at TiO_2 interface is crucial.

We finally close this article by highlighting the importance of Ni metallicity conservation and interface sharpness with regard to strain engineered magnetic properties in VANs. As put forward in the introduction, nanocolumnar composites are an ideal test bed to scrutinize magneto-elastic effects, due to their huge heterointerface. This especially holds true for transition-metal/oxide VANs, where the pronounced lattice mismatch between the oxide and metal species can induce large axial nanowire strains ε_{zz}, as recently demonstrated for Ni:STO.[26] In this study, a decreasing linear relationship between ε_{zz} and the nanowire radius r was evidenced. Thus, in principle, the reduction of r provides a simple strategy to achieve large magneto-elastic effects. However, it also results in an increase of the relative amount of interfacial Ni atoms, which can have a negative impact on the magnetic properties of the metallic phase, via oxidation or compound formation.[47] Similarly, partial interfacial mixing between lattice mismatched phases might induce lattice parameter accommodation, a detrimental effect, considering the quest for maximum strain. Efficient strain engineering in metal/oxide composites thus requires growth strategies that preserve the metallicity of the embedded wires and provide sharp metal/oxide interfaces. Both criteria are met in self-assembled Ni:STO columnar composites, and large values of the axial strain can be reached, as a consequence of the vertical epitaxy. The mean axial (ε_{zz}) and radial strain (ε_{rr}) within the 5-nm-diameter Ni nanowires were determined by x-ray diffraction measurements: ε_{zz}=2.4% and ε_{rr}=-0.3 %. This very large tensile strain along the wires axis should give rise to strong magneto-elastic effects, as will be examined in the remainder of the paper.

Figure 5(b) shows magnetic hysteresis loops acquired by measuring x-ray magnetic circular dichroism (XMCD) at the Ni L_3 edge, and by classical magnetometry. As can be seen, both loops are almost identical, indicating that the ferromagnetic behavior of the nanowires in vicinity of the surface is representative for the whole sample. Performing measurements in

TEY mode does not represent a limitation in the present case, and the analysis of angle-dependent XMCD signals can be considered representative for the whole sample. In the following, we define θ as the angle between the applied field and the axis of the wires. Figure 5(c) shows magnetic hysteresis loops acquired with the field applied along the nanowires axis (θ=0°) and perpendicular to this axis (θ=90°). Comparison of the cycles reveals that the remanence is larger for θ=90° than for θ=0°. Furthermore, the saturation field is weaker when the field is applied perpendicular to the wires axis. This indicates that the axis of the wires is not the magnetic easy axis. This is indeed confirmed by the results displayed in Figure 5(d), where the variation of the remanent magnetization as a function of θ is given. The remanent magnetization is a monotonous function of θ with a minimum value for θ=0. This indicates that the axis of the nanowires is a hard magnetic axis.

To analyze the magnetic properties of the present composite, two different anisotropy contributions have to be taken into consideration. First, there is a shape-induced term resulting from the high aspect ratio of the wires. This term is usually dominating in conventional magnetic nanowire arrays, typically obtained via electrodeposition into cylindrical nanopores, giving rise to an easy axis magnetic direction along the wire axis.[48] In the present system, the magnitude of this uniaxial shape anisotropy contribution is given by:

$$K_{ms} = \frac{\mu_0}{4} M_s^2 (1 - 3P)$$

where M_s is the saturation magnetization and P is the porosity (volume fraction occupied by the wires) of the NWs assembly.[49] Using a typical value of the porosity corresponding to samples studied in this work, P=10%, gives K_{ms}=5.3 10^4 J.m^{-3}. In addition, a strain induced anisotropy contribution has to be considered. Bulk Ni has a negative magnetostriction coefficient λ_{001}.[50] In the case of uniaxial strain ε_{zz} along [001], the uniaxial magnetoelastic contribution is given by:[51]

$$K_{me} = \frac{3}{2}\lambda_{001}(c_{11} - c_{12})(\varepsilon_{zz} - \varepsilon_{rr})$$

where c_{ij} are elastic constants.[52] Neglecting ε_{rr}, a reasonable approximation in the present case where the axial strain is much larger than the radial strain, the magnetoelastic contribution becomes:

$$K_{me} \cong \frac{3}{2}\lambda_{001}(c_{11} - c_{12})\varepsilon_{zz}$$

Because λ_{001} is negative in Ni, the total uniaxial anisotropy, $K=K_{ms}+K_{me}$, is the sum of two terms with opposite signs. K_{ms} is positive and favors a magnetic easy axis along the wire axis. K_{me} is negative and favors a magnetic hard axis along the wire axis. The two terms compete and the wires axis becomes a hard axis if $K<0$, *i.e.* if $K_{ms}<|K_{me}|$. This corresponds to the situation where ε_{zz} exceeds the critical value defined by:

$$\varepsilon_{crit} = \left|\frac{\mu_0 M_s^2(1-3P)}{6\lambda_{001}(c_{11} - c_{12})}\right| \cong 0.6\%$$

Since ε_{zz} exceeds ε_{crit}, the system exhibits a hard axis oriented along the wire axis, as clearly demonstrated by the results in Figure 5(c-d). Thus, these results confirm that the total uniaxial anisotropy has changed sign compared to the unstrained case. This provides clear experimental evidence for strong magneto-structural coupling in the Ni:STO VAN.

3. Conclusion

The structure and chemical composition of the vertical interface in a Ni:$SrTiO_3$ VAN could be determined by STEM and EELS measurements with atomic resolution. The obtained results demonstrate the absence of NiO and the metallic character of the last external atomic planes of the nanowires embedded in $SrTiO_3$. The full preservation of Ni metallicity is further

confirmed by x-ray absorption spectroscopy, and magnetic measurements indicate that in Ni:$SrTiO_3$ VANs the axis of the Ni wires is the hard magnetic axis due to strong magneto-elastic effects. This establishes Ni:$SrTiO_3$ as a model system for the study of strain-engineering of the magnetic anisotropy in VANs.

4. Experimental Section

Sample growth: Samples were grown by pulsed laser deposition (PLD) under high vacuum (base pressure 2.10^{-6} mbar) using NiO and $SrTiO_3$ (STO) targets and a quadrupled Nd:YAG laser (wavelength 266 nm) operating at 10 Hz with fluence in the 1-3 $mJ.cm^{-2}$ range. Growth was performed on $SrTiO_3$(001) single crystalline substrates held at 650°C. A sequential deposition scheme was adopted, as described in previous works.[20,26] NiO and STO targets are ablated sequentially, resulting in a succession of submonolayer deposition steps. This leads to the formation of the vertically aligned Ni nanowires embedded in the epitaxial $SrTiO_3$/$SrTiO_3$(001) matrix. The mean diameter of the nanowires can be tuned by adjusting the ratio of laser shots on NiO and STO targets during a sequence.[26] After completion of the sequential deposition steps, the samples were capped *in-situ* with an ultrathin AlO_x layer to prevent surface oxidation upon exposure to air. The structural properties of the samples were characterized by x-ray diffraction and transmission electron microscopy, in order to determine the epitaxial relationships and dimensions of the nanowires. Ni is found to grow epitaxially within the STO matrix with $(001)_{Ni}\|(001)_{STO}$ and $[100]_{Ni}\|[100]_{STO}$. In the samples studied in the present work, the Ni nanowires have mean diameters of 2.4 nm and 5 nm.

Sample analysis: Samples were thinned using a two-step method. The back side of the sample was first mechanically thinned until the thickness became less than a few tens of microns. Then, Ar-ion milling was used in order to reach the electron transparency. HAADF STEM images and STEM-EELS spectrum-images were obtained using a Nion Ultra-STEM MC

HERMES 100 microscope operating at 60 kV, equipped with a C5 Nion QO probe corrector, a monochromator[40] and a Gatan Enfinium spectrometer. EELS elemental maps are shown after principal component analysis[41] of a spectrum-image with dimensions 68×68×2048, acquired with an energy resolution of 350 meV, a beam current of 120pA, a dwell time of 0.2s/pixel, and a dispersion of 0.37 eV/ch. Qualitative elemental profiles were obtained by integrating EELS intensity maps across the nanowire. Energy-loss near-edge structure spectrum-images were acquired with an energy resolution of 160 meV, a beam current of 55 pA, a dispersion of 0.05 eV/ch, and dwell times of 0.20 s/pixel for the Ti-$L_{2,3}$ edges, 0.35 s/pixel for the O-*K* edge and 0.4 s/pixel for the Ni- $L_{2,3}$ edges. High signal to noise in images of Figure 2(b), Figure 4(a), S1(inset), and S2(a) were obtained after alignment of a stack of 42 images, using the built-in stack-alignment plugin in Gatan Digital Micrograph software. The convergence angle was ≈ 32 mrad, the HAADF collection angular range ≈ 85−195 mrad, and the EELS collection semi angles ≈ 44 mrad.

X-ray absorption spectroscopy and x-ray magnetic circular dichroism experiments were carried out on the DEIMOS beamline of SOLEIL synchrotron.[53–55] Data were acquired in total electron yield mode. The samples were kept under ultrahigh vacuum at 4.2 K during measurements. The applied magnetic field was collinear to the x-ray propagation vector. The incidence on the sample was set through a rotation of the sample by an angle θ. θ=0° refers to normal incidence. XAS and XMCD spectra were acquired at the Ni-$L_{2,3}$ edges by scanning the photon energy in the 840-880 eV range. Element-specific hysteresis loops were acquired by scanning the magnetic field at constant x-ray energy, set to the maximum of the XMCD signal, for left and right circular polarization. For the acquisition of XMCD spectra at remanence, the following scheme was used: the sample is submitted to a magnetic field exceeding the saturation field in the positive direction, the field is then set to zero and absorption spectra are recorded with left and right circular polarizations. The same procedure

is then applied with the saturating field in the opposite direction. The XMCD spectra at remanence are then obtained by properly averaging data recorded for both direction of application of the field. Magnetic hysteresis loops were also acquired using a vibrating sample magnetometer (VSM).

Supporting Information

Additional data extracted from EELS spectrum-images are provided. Figure S1 shows the chemical profiles extracted through the nanowire along a direction oriented at 45° with respect to the one used in Figure 3. Figure S2 shows a comparison of the Ti-$L_{2,3}$ and O-K edges fine structure obtained at the $[100]_{STO}\|[100]_{Ni}$ and the $[110]_{STO}\|[110]_{Ni}$ nanowire-matrix interfaces. Figure S3 compares the Ti-$L_{2,3}$ and Ni-$L_{2,3}$ edges fine structure obtained in the first atomic plane of the nanowire with bulk references obtained respectively in metallic Ti and Ni. Figure S4 illustrates the method employed to extract the Ni-L_3 to L_2 ratio from atomically resolved EELS data.

Acknowledgements

Scanning Transmission Electron Microscopy (STEM) experiments were carried out at Super-STEM, the EPSRC National Research Facility for Advanced Electron Microscopy. M. Bugnet and G. Radtke are grateful to SuperSTEM for hospitality and access to the microscopes. We acknowledge SOLEIL for provision of synchrotron radiation facilities and thank the staff of the MPBT platform of Sorbonne Université for their support. The authors also gratefully thank F. Breton for his assistance and design of the PLD control system. This work was supported by French state funds managed by the ANR within the Investissements d'Avenir

programme under reference ANR-11-IDEX-0004-02, and more specifically within the framework of the Cluster of Excellence MATISSE led by Sorbonne Universités. M. Bugnet acknowledges funding from INSA Lyon through the BQR fund THERMOS. M. Hennes acknowledges financial support from the French Embassy in Berlin (Service pour la Science et la Technologie) and Campus France. X. Weng gratefully acknowledges financial support of the Chinese Government Scholarship from China Scholarship Council (CSC No. 201608070062). This work has benefited from a funding from LabEx PALM (ANR-10-LABX-0039-PALM).

References

[1] J. L. MacManus-Driscoll, *Adv. Func. Mat.* **2010**, *20*, 2035.

[2] W. Zhang, A. Chen, Z. Bi, Q. Jia, J. L. MacManus-Driscoll, H.Wang, *Curr. Opin. Solid State Mater. Sci.* **2014**, *18*, 6.

[3] O. I. Lebedev, J. Verbeeck, G. Van Tendeloo, O. Shapoval, A. Belenchuk, V. Moshnyaga, B. Damashcke, K. Samwer, *Phys. Rev. B* **2002**, *66*, 104421.

[4] F. Vidal, Y. Zheng, P. Schio, F. J. Bonilla, M. Barturen, J. Milano, D. Demaille, E. Fonda, A. J. A. de Oliveira, V. H. Etgens, *Phys. Rev. Lett.* **2012**, *109*, 117205.

[5] A. Chen, Z. Bi, H. Hazariwala, X. Zhang, Q. Su, L. Chen, Q. Jia, J. L. MacManus-Driscoll, H. Wang, *Nanotechnology* **2011**, *22*, 315712.

[6] Q. Su, W. Zhang, P. Lu, S. Fang, F. Khatkhatay, J. Jian, L. Li, F. Chen, X. Zhang, J. L. MacManus-Driscoll, A. Chen, Q. Jia, H. Wang, *ACS Appl. Mater. Interfaces* **2016**, *8*, 20283.

[7] H. Zheng, J. Wang, S. E. Lofland, Z. Ma, L. Mohaddes-Ardabili, T. Zhao, L. Salamanca-Riba, S. R. Shinde, S. B. Ogale, F. Bai, D. Viehland, Y. Jia, D. G. Schlom, M. Wuttig, A. Roytburd, R. Ramesh, *Science* **2004**, *303*, 661.

[8] H. Zheng, F. Straub, Q. Zhan, P.-L. Yang, W.-K. Hsieh, F. Zavaliche, Y.-H. Chu, U. Dahmen, R. Ramesh, *Adv. Mater.* **2006**, *18*, 2747.

[9] H. Zheng, Q. Zhan, F. Zavaliche, M. Sherburne, F. Straub, M. P. Cruz, L.-Q. Chen, U. Dahmen, R. Ramesh, *Nano Lett.* **2006**, *6*, 1401.

[10] Q. Zhan, R. Yu, S. P. Crane, H. Zheng, C. Kisielowski, R. Ramesh, *Appl. Phys. Lett.* **2006**, *89*, 172902.

[11] N. Dix, R. Muralidharan, J.-M. Rebled, S. Estrade, F. Peiro, M. Varela, J. Fontcuberta, F. Sanchez, *ACS Nano* **2010**, *4*, 4955.

[12] H.-J. Liu, L.-Y. Chen, Q. He, C.-W. Liang, Y.-Z. Chen, Y.-S. Chien, Y.-H. Hsieh, S.-J. Lin, E. Arenholz, C.-W. Luo, Y. L. Chueh, Y. C. Chen,Y. H. Chu, *ACS Nano* **2012**, *6*, 6952.

[13] N. M. Aimon, D. H. Kim, H. K. Choi, C. A. Ross, *Appl. Phys. Lett.* **2012**, *100*, 092901.

[14] N. M. Aimon, D. H. Kim, H. K. Choi, X. Y. Sun, D. H. Kim, C. A. Ross, *Adv. Mater.* **2014**, *26*, 3063.

[15] S. Lee, J. L. MacManus-Driscoll, *APL Materials* **2017**, *5*, 0404.

[16] L. Mohaddes-Ardabili, H. Zheng, S. B. Ogale, B. Hannoyer, W. Tian, J. Wang, S. E. Lofland, S. R. Shinde, T. Zhao, Y. Jia, L. Salamanca-Riba, D. G. Schlom, M. Wuttig, R. Ramesh, *Nat. Mater.* **2004**, *3*, 533.

[17] F. Vidal, Y. Zheng, J. Milano, D. Demaille, P. Schio, E. Fonda, B. Vodungbo, *Appl. Phys. Lett.* **2009**, *95*, 152510.

[18] P. Schio, F. Vidal, Y.Zheng, J. Milano, E. Fonda, D. Demaille, B. Vodungbo, J.Varalda, A. J. A. de Oliveira, V. H. Etgens, *Phys. Rev. B* **2010**, *82*, 094436.

[19] J. Shin, A. Goyal, C. Cantoni, J. W. Sinclair, J. R. Thompson, *Nanotechnology* **2012**, *23*, 155602.

[20] F. J. Bonilla, A. Novikova, F. Vidal, Y. L. Zheng, E. Fonda, D. Demaille, V. Schuler, A. Coati, A. Vlad, Y. Garreau, M. Sauvage Simkin, Y. Dumont, S. Hidki, V. Etgens, *ACS Nano* **2013**, *7*, 4022.

[21] V. Schuler, J. Milano, A. Coati, A. Vlad, M. Sauvage-Simkin, Y. Garreau, D. Demaille, S. Hidki, A. Novikova, E. Fonda, Y. Zheng, F. Vidal, *Nanotechnology* **2016**, *27*, 495601.

[22] S. Kawasaki, R. Takahashi, T. Yamamoto, M. Kobayashi, H. Kumigashira, J. Yoshinobu, F. Komori, A. Kudo, M. Lippmaa, *Nat. Commun.* **2016**, *7*, 11818.

[23] L. Li, L. Sun, J. S. Gomez-Diaz, N. L. Hogan, P. Lu, F. Khatkhatay, W. Zhang, J. Jian, J. Huang, Q. Su, M. Fan, C. Jacob, J. Li, X. Zhang, Q. Jia, M. Sheldon, A. Alu, X. Li, H. Wang, *Nano Lett.* **2016**, *16*, 3936.

[24] J. Huang, L. Li, P. Lu, Z. Qi, X. Sun, X. Zhang, H. Wang, *Nanoscale* **2017**, *9*, 7970.

[25] M. Hennes, V. Schuler, X. Weng, J. Buchwald, D. Demaille, Y. Zheng, F. Vidal, *Nanoscale* **2018**, *10*, 7666.

[26] X. Weng, M. Hennes, A. Coati, A. Vlad, Y. Garreau, M. Sauvage-Simkin, E. Fonda, G. Patriarche, D. Demaille, F. Vidal, Y. Zheng, *Phys. Rev. Materials* **2018**, *2*, 106003.

[27] J. L. MacManus-Driscoll, P. Zerrer, H. Wang, H. Yang, J. Yoon, A. Fouchet, R. Yu, M. G. Blamire, Q. Jia, *Nat. Mater.* **2008**, *7*, 314.

[28] A.Chen, Q. Su, H. Han, E. Enriquez, Q. Jia, *Adv. Mater.* **2018**, *31*, 1803241.

[29] D.-M. Kepaptsoglou, K. Hadidi, O.-M. Løvvik, A. Magraso, T. Norby, A. E. Gunnæs, A. Olsen, Q. M. Ramasse, *Chem. Mater.* **2012**, *24*, 4152.

[30] L. Bocher, A. Gloter, A. Crassous, V. Garcia, K. March, A. Zobelli, S. Valencia, S. Enouz-Vedrenne, X. Moya, N. D. Marthur, C. Deranlot, S. Fusil, K. Bouzehouane, M. Bibes, A. Barthélémy, C. Colliex, O. Stéphan, *Nano Lett.* **2012**, *12*, 376.

[31] R. F. Egerton, *Electron Energy Loss Spectroscopy in the Electron Microscope*, 3rd ed., Springer, New York, NY, USA **2011**.

[32] F. M. F. De Groot, J. Faber, J. J. M. Michiels, M. T. Czyżyk, M. Abbate, J. C. Fuggle, *Phys. Rev. B* **1993**, *48*, 2074.

[33] F. M. F. De Groot, J. C. Fuggle, B. T. Thole, G. A. Sawatzky, *Phys. Rev. B* **1990**, *41*, 928.

[34] K. Van Benthem, C. Elsässer, M. Rühle, *Ultramicroscopy* **2003**, *96*, 509.

[35] T. Mizoguchi, J. P. Buban, K. Matsunaga, T. Yamamoto, Y. Ikuhara, *Ultramicroscopy* **2006**, *106*, 92.

[36] P. L. Potapov, S. E.Kulkova, D. Chryvers, J. Verbeeck, *Phys. Rev. B* **2001**, *64*, 184110.

[37] P. Ewels, T. Sikora, V. Serin, C. P. Ewels, L. A. Lajaunie, *Microsc. Microanal.* **2016**, *22*, 717.

[38] S. L. Dudarev, G. A. Botton, S. Y. Savrasov, C. J. Humphreys, A. P. Sutton, *Phys. Rev. B* **1998**, *57*, 1505.

[39] K. van Benthem, C. Scheu, W. Sigle, M. Z. Rühle, *Metallkd.* **2002**, *93*, 362.

[40] O. L. Krivanek, T. C. Lovejoy, N. Dellby, R.W. Carpenter, *Microscopy* **2013**, *62*, 3.

[41] L. Lucas, P. Burdet, M. Cantoni, C. Hébert, *Micron* **2013**, *52*, 49.

[42] C. T. Chen, N. V. Smith, F. Sette, *Phys. Rev. B* **1991**, *43*, 6785.

[43] Y. Ufuktepe, G. Akgül, F. Aksoy, D. Nordlund, *X-Ray Spectrometry* **2011**, *40*, 427.

[44] X. Zhang, A. A. Demkov, *J. Vac. Sci. Technol. B* **2002***, 20,* 1664.

[45] A. Staykov, H. Tellez, J. Druce, J. Wu, T. Ishihara, J. Kilner, *Sci. Technol. Adv. Mater* **2018**, *19*, 221.

[46] A. D. Polli, T. Wagner, T. Gemming, M. Rühle, *Surf. Sci.* **2000**, *448*, 279.

[47] L. Favre, V. Dupuis, E. Bernstein, P. Mélinon, A. Pérez, S. Stanescu, T. Epicier, J.-P. Simon, D. Babonneau, J.-M. Tonnerre, J.-L. Hodeau, *Phys. Rev. B* **2006**, *74*, 014439.

[48] K. Nielsch, R. B. Wehrspohn, J. Barthel, J. Kirschner, U. Gösele, S. F. Fischer, H. Kronmüller, *Appl. Phys. Lett.* **2001**, *79*, 1360.

[49] A. Encinas-Oropesa, M. Demand, L. Piraux, I. Huynen, U. Ebels, *Phys. Rev. B* **2001**, *63*, 104415.

[50] S. Kadowaki, M. J. Takahashi, *Phys. Soc. Jap.***1981**, *50*, 1154.

[51] C. Kittel, *Rev. Mod. Phys.* **1949**, *21*, 541.

[52] H. J. Leamy, H. Warlimont, *Phys. Stat. Sol. B* **1970**, *37*, 523.

[53] P. Ohresser, E. Otero, F. Choueikani, K. Chen, S. Stanescu, F. Deschamps, T. Moreno, F. Polack, B. Lagarde, J.-P. Daguerre, F. Marteau, F. Scheurer, L. Joly, J.-P. Kappler, B. Muller, O. Bunau, Ph. Sainctavit, *Rev. Sci. Instrum.* **2014**, *85*, 013106.

[54] L. Joly, E. Otero, F. Choueikani, F. Marteau, L. Chapuis, P. Ohresser, *J. Synchrotron Radiat.* **2014**, *21*, 502.

[55] J.-P. Kappler, E. Otero, W. Li, L. Joly, G. Schmerber, B. Muller, F. Scheurer, F. Leduc, B. Gobaut, L. Poggini, G. Serrano, F. Choueikani, E. Lhotel, A. Cornia, R. Sessoli, M. Mannini, M.-A. Arrio, Ph. Sainctavit, P. Ohresser, *J. Synchrotron Radiat.* **2018**, *25*, 1727.

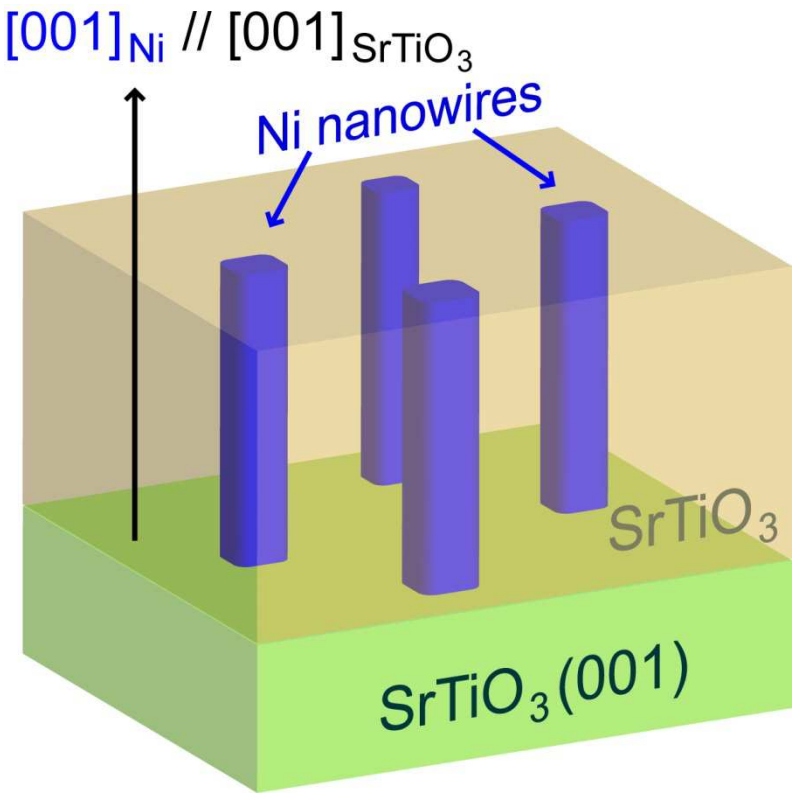

Figure 1. Schematics of a Ni:$SrTiO_3$/$SrTiO_3$(001) epitaxial VAN structure.

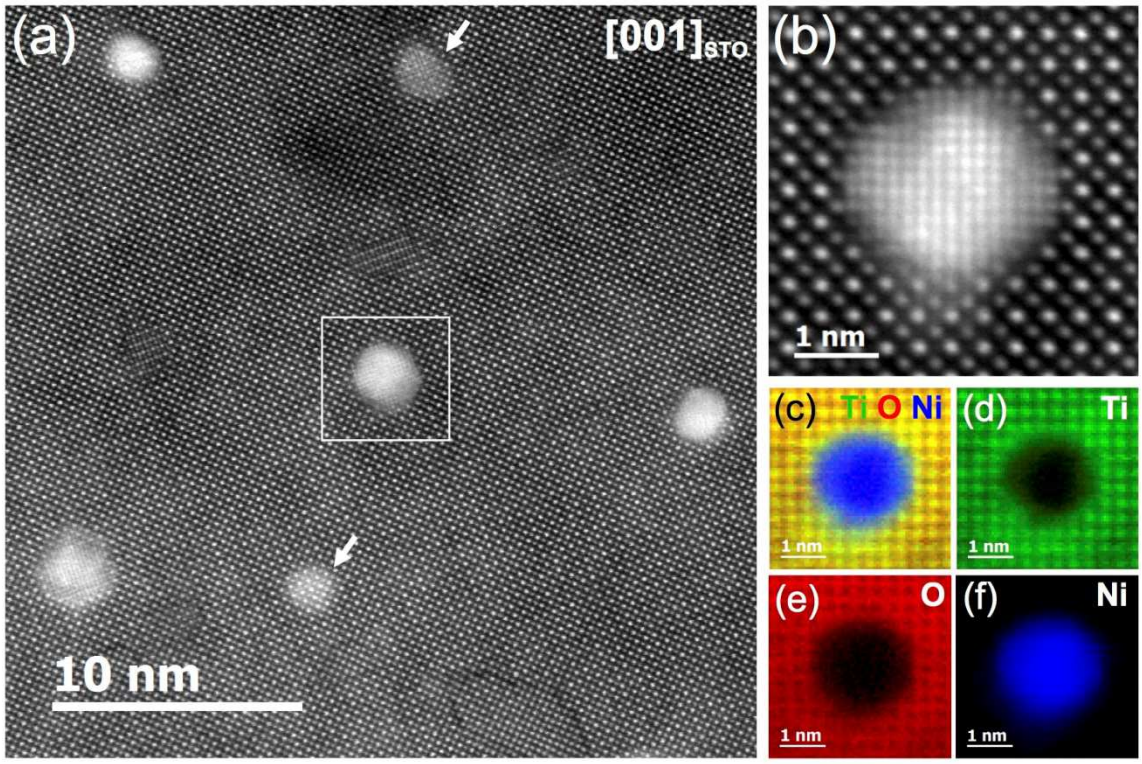

Figure 2. (a) Global HAADF top view, along [001] zone axis, of the sample showing a few Ni nanowires in the STO matrix. The STO and Ni lattices appear superimposed for short nanowires, as indicated by arrows, in which case the top or bottom surface of the thinned sample does not intersect the nanowires. Detailed analysis of a typical nanowire of diameter 2 nm: (b) high-resolution HAADF image obtained after alignment of a stack of 42 images, showing the atomic structure of the nanowire; (c) composite chemical map of the nanowire built from the elemental Ti map shown in (d), O map in (e) and Ni map in (f) extracted from the Ti-$L_{2,3}$ edges (~457eV), the O-K edge (~531eV) and the Ni-$L_{2,3}$ edges (~855eV) respectively. All maps are displayed after noise removal through principal component analysis (PCA). Variations of the intensity with the STO lattice periodicity is visible on the Ti and O maps but not in the Ni nanowire due to the smaller lattice spacing in the metal.

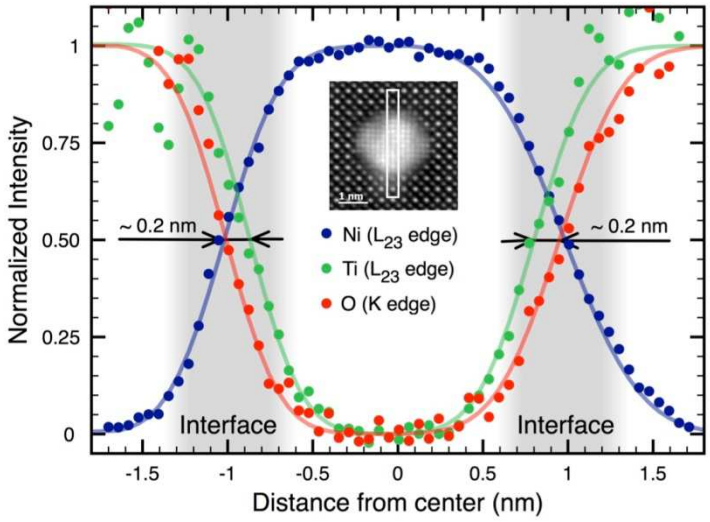

Figure 3. Ni, Ti and O chemical profiles across the nanowire extracted from elemental maps, obtained by integrating EELS signal in the box shown in inset. Intensities are normalized to the same maximum height. According to the Ni profile, the projected diameter of the nanowire is close to 2nm. The slightly wider O profile compared to Ti indicate a Ti-rich interface. The points correspond to the experimental data while the lines are just guides for eye.

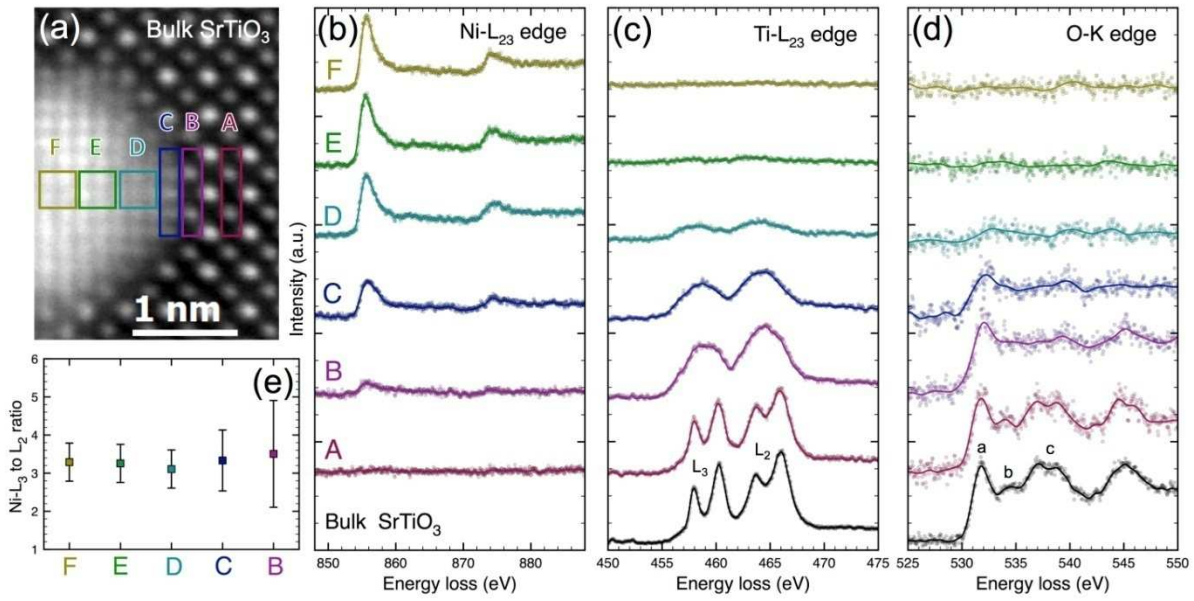

Figure 4. Atomic and electronic structure of the nanowire-matrix $[100]_{STO}\|[100]_{Ni}$ interface. (a) High-resolution HAADF image of the interface between the Ni nanowire and the $SrTiO_3$ matrix, boxes indicate the spectrum-image integration areas used to obtain the spectra shown in (b) for the Ni-$L_{2,3}$ edges, (c) for the Ti-$L_{2,3}$ edges and (d) for the O-K edge. (e) Ni-L_3 to L_2 ratio obtained from the spectra displayed in (b). The points correspond to the experimental data while the lines are just guides for eye.

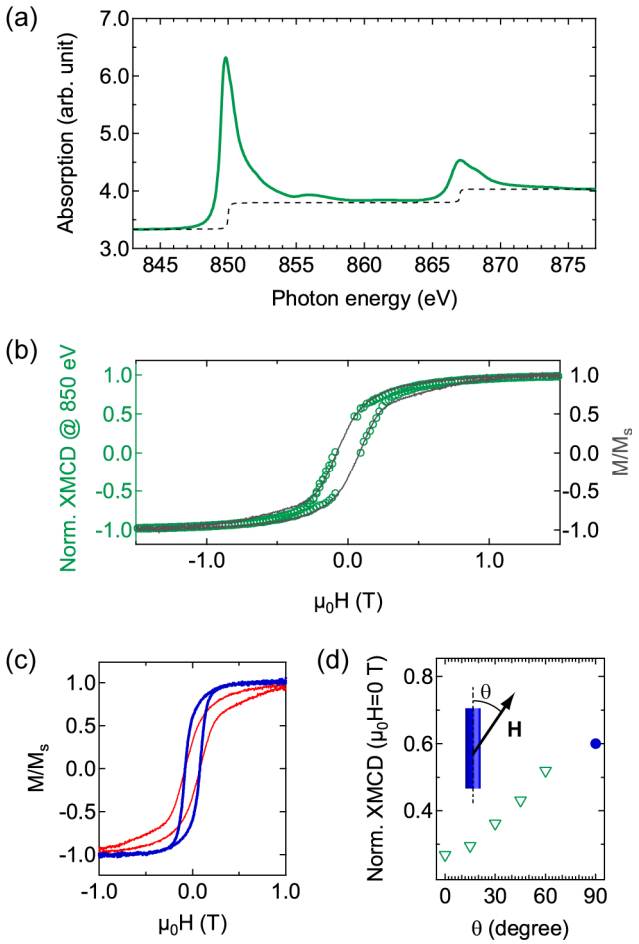

Figure 5. X-ray absorption spectroscopy and magnetic measurements of Ni nanowires assembly in STO, measured at the Ni-$L_{2,3}$ edges. (a) X-ray absorption spectrum. (b) Magnetic hysteresis loops acquired with the magnetic field applied along the Ni nanowires axis as measured by XMCD at the Ni-L_3 edge (symbols) and using a vibrating sample magnetometer (line). (c) Magnetic hysteresis loops acquired with the magnetic field applied along the Ni nanowires axis (thin line) and perpendicular to the axis (thick line) using a vibrating sample magnetometer. (d) Triangle: XMCD at the Ni-L_3 edge, measured at remanence, as a function of the angle θ between the nanowires axis and the applied magnetic field (θ=0 corresponds to a field applied along the axis of the nanowires). Disk: value of the normalized remanence for θ=90° deduced from vibrating sample magnetometer measurements.